Stress fibers are embedded in a contractile cortical network.

Timothée Vignaud[1,2,3], Calina Copos[4], Christophe Leterrier[5], Mauricio Toro-Nahuelpan[6], Qingzong Tseng[1,2], Julia Mahamid[6], Laurent Blanchoin[1,2], Alex Mogilner[4]*, Manuel Théry[1,2]* and Laetitia Kurzawa[1,2]*

[1] CytoMorpho Lab, Laboratoire de Physiologie cellulaire et Végétale, Interdisciplinary Research Institute of Grenoble, CEA, CNRS, INRA, Grenoble-Alpes University, Grenoble, France.
[2] CytoMorpho Lab, Human Immunology Physiopathology and Immunotherapy, Institut de Recherche Saint Louis, University of Paris, CEA, INSERM, F-75475, Paris, France.
[3] Clinique de chirurgie digestive et endocrinienne, Hôtel Dieu, Nantes, 44093, France.
[4] Courant Institute and Department of Biology, New York University, New York, NY, United States of America.
[5] Aix Marseille Université, CNRS, INP UMR7051, NeuroCyto, Marseille, France.
[6] Structural and Computational Biology Unit, European Molecular Biology Laboratory (EMBL), 69117 Heidelberg, Germany.

SUPPLEMENTARY INFORMATION

- Supplementary methods
- Supplementary references
- Supplementary Videos

Supplementary methods

Model description

The actin cytoskeletal meshwork is modeled as a two-dimensional deformable elastic material [1–6]. This is a simplification of a three-dimensional model since on average the height of an adherent cell is much smaller than its in-plane dimensions, and so we neglect any out-of-plane deformations. The rheology of the cytoskeleton meshwork has been described as a viscoelastic gel with time-evolving material properties due to the turnover of actin and action of molecular motors [7–9]. There are two possible theoretical descriptions used to capture this rheology: (a) elastic elements embedded in a viscous gel [10,11], or (b) viscous elements embedded in an elastic gel [4,12,13]. The loss of traction force due to an ablation suggests that on timescales of tens of seconds the material response is well described by an elastic gel with viscous elements (Figure 1f). Further, it has been reported that the viscous timescale of the actin gel due to the growth and reorganization of actin filaments (order of minutes) is much longer than our observation time [7,9].

For simplicity, the elastic gel is coarse-grained into a network of nodes interconnected by elastic springs, while viscous elements are excluded as their dynamics would only affect the transient behavior [4,14]. An interconnected network of nodes and elastic links is a general theoretical approach used in previously published models to describe the mechanics of the cell interior of motile and adherent cells [1,2,4–6]. While continuum approaches have been developed and successfully used as well [10,12,15], there is a tradition of modeling the cytoskeletal meshwork using discrete elements: nodes and springs [16].

Specifically, in the model, the cell interior is a two-dimensional rectangular network of nodes connected by Hookean elastic springs. The endpoints of the rectangular network are adhering to the substrate following experimental evidence (Figure 3a). The nodes represent material points of the cortical meshwork, while the elastic springs interconnecting the nodes model the mechanical response of the actin filament arrays. In the experiments with a dumbbell adhesive micropattern, large contractile actomyosin bundles are reported along the cell periphery stretching between the adhesive endpoints (Figure 1b). We include these bundles as additional nodes placed along a line at the top and bottom interface of the rectangular elastic meshwork. The nodes representing the actomyosin bundles are interconnected by Hookean elastic springs with an additional tension to mimic the effect of myosin-generated contractility. The nodes are also connected to the meshwork via additional linear elastic links. The endpoints of the contractile fibers are anchored to the substrate as was done with the endpoints of the elastic meshwork. Our theoretical model is similar in spirit to the model reported in [17]: in both models, the cortical meshwork is discretized into a network of interconnected nodes and deformable elements, however our elements are elastic, while in [17], these elements are not Hookean springs, but rather ‘cables’ – springs that do not respond to compression.

At the beginning of the simulation, the initial network of nodes and springs is the result of a Delaunay triangulation algorithm applied to a rectangular domain. The nodes are chosen to be the vertices of the triangulation and the elastic springs are along the edges of the triangulation. All springs are created in an undeformed state. The linear springs in the meshwork are characterized by a stiffness k_1, while the additional links representing the actomyosin bundles have spring stiffness k_2 and tension γ_2. The connectors between the contractile fibers and the elastic meshwork have the same spring stiffness as the meshwork k_1.

Given this initial shape, elastic forces are computed at every node in the network. As was done previously [1,10], we assume that adhesion complexes generate viscous resistance to the deformation of the meshwork. The respective resistive force is given by $\xi\vec{u}$ where ξ is the effective adhesion drag coefficient and $\vec{u}$ is the velocity of the network in the lab coordinate system. The adhesion resistive force is balanced by the active elastic stresses: $\xi\vec{u} = \vec{F}$ at every material point. The elastic force at the material point is denoted by $\vec{F}$. At each time step, elastic forces are computed in the entire meshwork and the velocity of each node is determined from the force balance. At the endpoints of the rectangular network, the velocity is enforced to be zero since the cell is adhering to the substrate at these locations. Once the position of the nodes is updated in time, elastic forces are re-computed at these new locations and the algorithm proceeds as indicated above. Because of the relatively small deformations we never observe instabilities or crossovers in the triangulation. When the network achieves mechanical equilibrium, the forces exerted by the meshwork on the substrate (i.e., at the endpoints) are recorded as traction forces and qualitatively compared with experiments.

The scope of this theoretical framework is to probe the respective contribution of actomyosin bundled stress fibers, the internal cortical meshwork, and their mechanical coupling on exerted traction forces. The investigation is achieved by qualitative comparison of model predictions of the spatiotemporal distribution of traction forces and experimental measurements from adherent cells.

The values of the parameters were not taken from the literature, as there is a great variation in mechanical parameters reported in the published data due to significant mechanical differences in cell types, states and mechanochemical environments, as well as in experimental assays reported in multiple publications. Rather, we obtained model parameters from fits to one part of the experimental data, specifically to the measured values of the force loss due to a single cut along a stress fiber and of the force loss due to ablation. The rest of the data shows very good quantitative agreement with the predicted numerical experiments, without any additional changes in the parameter values (the number of parameters is also very small), which is a strong argument for the model validity. Moreover, as all measurements deal with the fraction of the force/energy loss, rather than with absolute dimensional force/energy values, we do not need the dimensional parameter values in the model. Rather, for computations, we normalize the parameters so that $k_1 = 1$ for the stiffness of the elastic network and the stiffness of the connections between the elastic meshwork and the contractile fibers.

For the contractile fibers we choose a larger spring stiffness of $k_2 = 20$ and tension $\gamma_2 = 2$ relative to the normalized stiffness of the elastic mesh. The value for the spring stiffness k_2 is chosen to qualitatively reproduce the force loss for two consecutive cuts along the same fiber; specifically, the difference in the force released between the two cuts would be less significant by increasing k_2. In the modified model with a contractile cortical meshwork, we found that decreasing k_2 results in too much force loss in the region of the cell opposite of the injured stress fiber. The value for the tension in the stress fiber, γ_2, is arbitrarily chosen – numerical experiments have shown that we can reproduce the data by varying γ_2 in the wide range – but its value relative to γ_1 is important. First, indifferent of our numeric choices for the stress fiber parameters, k_2 and γ_2, in the absence of a tension in the meshwork (i.e., $\gamma_1 = 0$) ablation of the mesh would never produce a force loss (Figure 3g). Second, introducing too large of a tension in the meshwork would imply that cuts along the fiber release very little force. To introduce cortical tension, we set $\gamma_1 = 0.5 = 0.25\gamma_2$ to simultaneously reproduce the force loss due to a single cut along a stress fiber and force loss due to an ablation of the cortical network. In particular, there are two competing effects that limit the choice of γ_1 — increasing γ_1 increases the force released with ablation since the cortical mesh participates more in generating contraction, but increasing γ_1 decreases the force released with a single cut on the fiber as then, the stress fibers contribute more to the force of the entire system. To balance these competing effects and match the force loss in ablation and single cut observed in experiments, we fix γ_1 = 0.25*γ_2. Furthermore, we varied each of the two parameters, k_2, γ_2, individually, tenfold and chosen to match as close as possible the qualitative behavior seen in the experiments. The drag coefficient is 0.025 arbitrary force per velocity units (2 orders of magnitude smaller than the elastic forces). Because traction forces are computed after the meshwork relaxes to the equilibrium, the value of the drag coefficient does not affect our results. The time step is $\Delta t = 0.0001$ arbitrary time units and is chosen to meet numerical stability constraints.

At each discretized location in the cortical meshwork, Newton's second law is the governing equation of the system:

$$\xi \vec{u} = \vec{F} \quad (1)$$

where ξ is the effective adhesion drag coefficient and $\vec{u}$ is the velocity in the lab coordinate system. The elastic force at every discretized location is represented by $\vec{F}$.

We introduced stochastic noise in the model by assuming that the parameters for tensions and elasticity in the network vary randomly in space. Specifically, these parameters (mechanical characteristics of each deformable element in the network) are independent random draws from standard normal distributions centered around the baseline value with some variance, e.g.

$$f(\gamma_1) = \frac{1}{\sigma\sqrt{2\pi}} e^{-\frac{1}{2}\left(\frac{x-\gamma_1^0}{\sigma}\right)^2} \quad (2)$$

where γ_1^0 is the baseline value for tension in the interior cytoskeletal mesh, and $\sigma = \gamma_1^0/3$ is the standard deviation. When this spatial noise is introduced in all parameters (both tensions and elasticities) in the entire network, we find that the qualitative trends observed in the deterministic model persist. Namely, less force is lost with shaving rather than a cut along a stress fiber, and a second consecutive cut along the same stress fibers results in less force loss on average. Similar results from simulations when the spatial mechanical noise is introduced only in elastic parameters (while contractility is constant), or only in contractile stresses (while elasticity is homogeneous).

Fig. 4d. single cut along SF

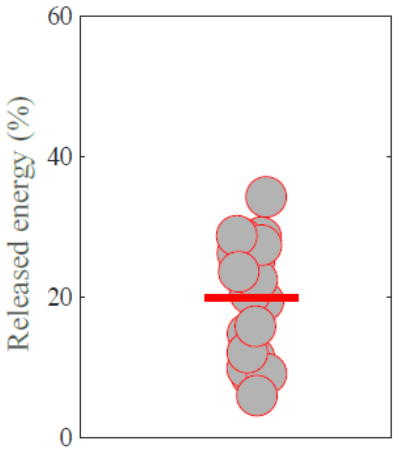

Fig. 4e. shaving

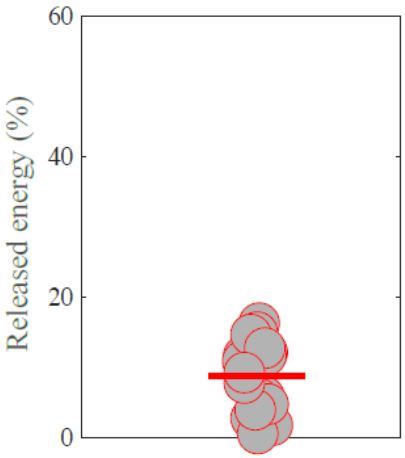

Fig. 4f. two cuts along same SF

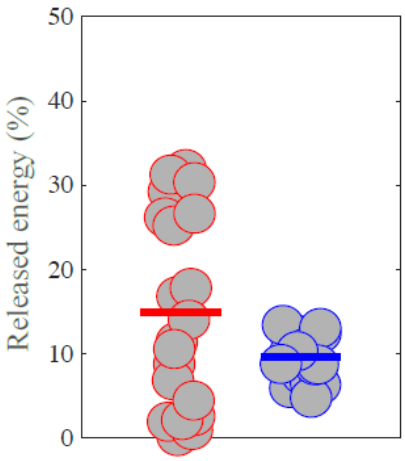

Statistics:

mean	19.87%	8.80%	14.98% | 9.69%
standard deviation	8.30%	4.83%	11.51% | 2.50%
# samples	20	20	20

Cryo-electron tomography

Wedge preparation by cryo-focused ion beam (cryo-FIB) milling was performed on a dedicated Aquilos dual-beam microscope (ThermoFisher Scientific, Brno, Czech Republic) as described in [18]. Appropriate positions for FIB preparations were identified and recorded in the MAPS 3.3 software (ThermoFisher Scientific, Brno, Czech Republic), and the eucentric height refined per position. Wedges were prepared using Gallium ion beam at 30 kV and stage tilt angles of 12°-13°, and conducted in a stepwise manner, starting 5 µm away from the area of interest with currents of 1 nA, gradually reduced to a current of 50 pA for the final cleaning steps. The grids were sputter coated after wedge preparation with platinum (10 mA, 3 s). Cryo-electron microscopy data were collected on a Titan Krios microscope operated at 300 kV (ThermoFisher Scientific, Eindhoven, Netherlands) equipped with a field-emission gun, a Quantum post-column energy filter (Gatan, Pleasanton, CA, USA), a K2 Summit direct detector camera (Gatan) and a Volta phase plate (VPP; ThermoFisher Scientific, Eindhoven, Netherlands). Data were recorded in dose-fractionation mode using acquisition procedures in SerialEM software v3.7.2 [19]. Prior to the acquisition of tilt-series, montages of the wedges were acquired at ~2 nm/pix. Tilt-series using a dose symmetric scheme [20] were collected in nano-probe mode, EFTEM magnification 42,000x corresponding to pixel size at the specimen level of 3.37 Å, 3-4 µm defocus, tilt increment 2° with constant dose of 2 e−/Å2 for all tilts, with a Volta Phase Plate.

Seven tomograms acquired from 2 wedges are presented, equivalent to 2 cells grown on dumbbell-shape micropatterns. The thickness of each tomogram (max./min.) was: P1: ~200/40 nm (Figure 5 and Extended Data 5 c, f); P2: ~200/80 nm (Extended Data 5 d, g); P3: ~190/70 nm (Fig. S5 e, h); P4: 320/285 nm (Fig. S5 b inset); in the second wedge was (Extended Data 5 j, k): ~200/160nm. Tomograms were reconstructed using the IMOD software package v 4.9.0 [19] as per [18], and filtered with an anisotropic nonlinear diffusion denoising algorithm (K value of 1, and 10 iterations).

Filament tracing was performed on tomograms binned to 13.48 Å pixel size, with the Amira software Amira XTracing Extension 6.7.0 (Thermo Fisher Scientific) as previously reported [21,22]. To reduce false positives, segmented actin structures with lengths below 70 nm were filtered out [23].

Supplementary references

1. Copos, C. A. *et al.* Mechanosensitive Adhesion Explains Stepping Motility in Amoeboid Cells. *Biophys. J.* **112**, 2672–2682 (2017).
2. Guthardt Torres, P., Bischofs, I. & Schwarz, U. S. Contractile network models for adherent cells. *Phys. Rev. E* **85**, 1–13 (2012).
3. Köhler, S. & Bausch, A. R. Contraction Mechanisms in Composite Active Actin Networks. *PLoS One* **7**, e39869 (2012).
4. Zhu, J. & Mogilner, A. Mesoscopic Model of Actin-Based Propulsion. *PLoS Comput. Biol.* **8**, e1002764 (2012).
5. Besser, A., Colombelli, J., Stelzer, E. H. K. & Schwarz, U. S. Viscoelastic response of contractile filament bundles. *Phys. Rev. E* **83**, 051902 (2011).
6. Bischofs, I. B., Klein, F., Lehnert, D., Bastmeyer, M. & Schwarz, U. S. Filamentous network mechanics and active contractility determine cell and tissue shape. *Biophys. J.* **95**, 3488–96 (2008).
7. Moeendarbary, E. *et al.* The cytoplasm of living cells behaves as a poroelastic material. *Nat. Mater.* **12**, 1–9 (2013).
8. Mofrad, M. R. K. Rheology of the Cytoskeleton. *Annu. Rev. Fluid Mech.* **41**, 433–453 (2009).
9. Gardel, M. L., Kasza, K. E., Brangwynne, C. P., Liu, J. & Weitz, D. a. Chapter 19: Mechanical response of cytoskeletal networks. *Methods Cell Biol.* **89**, 487–519 (2008).
10. Barnhart, E. L., Lee, K.-C., Allen, G. M., Theriot, J. a. & Mogilner, A. Balance between cell−substrate adhesion and myosin contraction determines the frequency of motility initiation in fish keratocytes. *Proc. Natl. Acad. Sci.* **112**, 201417257 (2015).
11. Larripa, K. & Mogilner, A. Transport of a 1D viscoelastic actin–myosin strip of gel as a model of a crawling cell. *Phys. A Stat. Mech. its Appl.* **372**, 113–123 (2006).
12. Joanny, J. & Prost, J. Active gels as a description of the actin-myosin cytoskeleton. *HFSP J.* **3**, 94–104 (2009).
13. Strychalski, W., Copos, C. A., Lewis, O. L. & Guy, R. D. A poroelastic immersed boundary method with applications to cell biology. *J. Comput. Phys.* **282**, 77–97 (2015).
14. Zimmermann, J., Enculescu, M. & Falcke, M. Leading-edge–gel coupling in lamellipodium motion. *Phys. Rev. E* **82**, 051925 (2010).
15. Oakes, P. W., Banerjee, S., Marchetti, M. C. & Gardel, M. L. Geometry Regulates Traction Stresses in Adherent Cells. *Biophys. J.* **107**, 825–833 (2014).
16. Boal, D. *Mechanics of the Cell*. (Cambridge University Press, 2012). doi:10.1017/CBO9781139022217
17. Paul, R., Heil, P., Spatz, J. P. & Schwarz, U. S. Propagation of mechanical stress through the actin cytoskeleton toward focal adhesions: Model and experiment. *Biophys. J.* **94**, 1470–1482 (2008).
18. Toro-Nahuelpan, M. *et al.* Tailoring cryo-electron microscopy grids by photo-micropatterning for in-cell structural studies. *Nat. Methods* **17**, 50–54 (2020).
19. Kremer, J. R., Mastronarde, D. N. & McIntosh, J. R. Computer Visualization of Three-Dimensional Image Data Using IMOD. *J. Struct. Biol.* **116**, 71–76 (1996).
20. Hagen, W. J. H., Wan, W. & Briggs, J. A. G. Implementation of a cryo-electron tomography tilt-scheme optimized for high resolution subtomogram averaging. *J. Struct. Biol.* **197**, 191–198 (2017).

21. Mahamid, J. *et al.* Visualizing the molecular sociology at the HeLa cell nuclear periphery. *Science (80-.).* **351**, 969–972 (2016).
22. Jasnin, M. *et al.* The Architecture of Traveling Actin Waves Revealed by Cryo-Electron Tomography. *Structure* **27**, 1211-1223.e5 (2019).
23. Rigort, A. *et al.* Automated segmentation of electron tomograms for a quantitative description of actin filament networks. *J. Struct. Biol.* **177**, 135–144 (2012).

Supplementary Videos

Video 1
Illustrations of stress fiber ablation (showed with white arrow heads) in nine cells plated on dumbbell-shaped micropatterns on poly-acrylamide gels. Scale bar is 10 μm.

Video 2
Illustration of stress fiber ablation and the measurement of the corresponding traction force field relaxation in a cells plated on dumbbell-shaped micropatterns on poly-acrylamide gel. Scale bar is 10 μm.

Video 3
Illustration of stress fiber shaving (in between the two tilted arrow heads) and the measurement of the corresponding traction force field relaxation in a cells plated on dumbbell-shaped micropatterns on poly-acrylamide gel. Scale bar is 10 μm.

Video 4
Illustrations of stress fiber shaving (in between the two tilted arrow heads) followed by stress fiber ablation (single vertical arrow head) and the measurement of the corresponding traction force field relaxation in a cells plated on dumbbell-shaped micropatterns on poly-acrylamide gel. Scale bar is 10 μm.

Video 5
Cryo-electron tomography of a stress fiber of a cryo-FIB-treated cell grown on a dumbbell-shape micropattern. Tomographic volume of a cryo-FIB generated wedge of an RPE1 cell grown on a dumbbell-shape pattern. Each slice is 6.8 nm thick. Video related to Figure 5b and Extended Data 5c and f wedge 1, position 1 (P1).

Video 6
Live imaging of RPE1-LifeAct-GFP cells on tripod-shaped micropattern showing the global and permanent remodelling of network architecture, suggestive of a complex interplay of longitudinal and lateral forces on cytoplasmic bundles. Time is indicated in hours and minutes. Scale bar = 20 μm.

Video 7
Live imaging of RPE1-LifeAct-GFP cells on tripod-shaped micropattern highlighting network reconfiguration by lateral translocation of cytoplasmic bundles in the absence of anchorage displacement (red arrows). Time is indicated in hours and minutes. Scale bar = 20 μm.

Video 8

Live imaging of RPE1-LifeAct-GFP cells on tripod-shaped micropattern revealing the emergence of cytoplasmic bundles from the cortical meshwork (in between red arrows) and the lateral expansion of a bundle, its splaying into a wider structure (orange arrows) and its re-coalescence into several adjacent bundles (magenta arrows). Time is indicated in hours and minutes. Scale bar = 20 μm.